RESEARCH ARTICLE

Key Points:
- New crustal constraints beneath the northern Transantarctic Mountains (TAMs)
- Crust thickens from ~20 km near the coast to ~41 km inland
- Locally thicker crust may explain additional topography in the northern TAMs

Crustal structure beneath the Northern Transantarctic Mountains and Wilkes Subglacial Basin: Implications for tectonic origins

Samantha E. Hansen[1], Lindsey M. Kenyon[1], Jordan H. Graw[1], Yongcheol Park[2], and Andrew A. Nyblade[3]

[1]Geological Sciences Department, University of Alabama, Tuscaloosa, Alabama, USA, [2]Korea Polar Research Institute, Incheon, Korea, [3]Geosciences Department, Pennsylvania State University, University Park, Pennsylvania, USA

Abstract The Transantarctic Mountains (TAMs) are the largest noncollisional mountain range on Earth. Their origin, as well as the origin of the Wilkes Subglacial Basin (WSB) along the inland side of the TAMs, has been widely debated, and a key constraint to distinguish between competing models is the underlying crustal structure. Previous investigations have examined this structure but have primarily focused on a small region of the central TAMs near Ross Island, providing little along-strike constraint. In this study, we use data from the new Transantarctic Mountains Northern Network and from five stations operated by the Korea Polar Research Institute to investigate the crustal structure beneath a previously unexplored portion of the TAMs. Using S wave receiver functions and Rayleigh wave phase velocities, crustal thickness and average crustal shear velocity ($\overline{V}_s$) are resolved within ±4 km and ±0.1 km/s, respectively. The crust thickens from ~20 km near the Ross Sea coast to ~46 km beneath the northern TAMs, which is somewhat thicker than that imaged in previous studies beneath the central TAMs. The crust thins to ~41 km beneath the WSB. $\overline{V}_s$ ranges from ~3.1–3.9 km/s, with slower velocities near the coast. Our findings are consistent with a flexural origin for the TAMs and WSB, where these features result from broad flexure of the East Antarctic lithosphere and uplift along its western edge due to thermal conduction from hotter mantle beneath West Antarctica. Locally, thicker crust may explain the ~1 km of additional topography in the northern TAMs compared to the central TAMs.

1. Introduction

The Transantarctic Mountains (TAMs) are a ~4000 km long mountain range that separate the East Antarctic craton from the West Antarctic Rift System (Figure 1) [*Robinson and Splettstoesser*, 1984]. Elevations in the TAMs reach up to 4500 m, making them comparable in both length and elevation to the Rocky Mountains [*Enright*, 2010]; however, unlike most mountain ranges of similar size, the TAMs show no evidence for a collisional origin. Apatite fission track dating indicates that the main phase of TAMs uplift occurred ~55 Ma, and the stratigraphic layers within the TAMs that predate this uplift remain nearly horizontal [*Fitzgerald et al.*, 1986]. The Wilkes Subglacial Basin (WSB; Figure 1), a down warp in the subglacial topography, parallels the TAMs on their inland side. Various origin mechanisms have been proposed for both the TAMs and the WSB, but additional observations are needed to further understand their tectonic history. Specifically, the crustal structure beneath the TAMs and the WSB is a key component to differentiating between formation mechanisms.

Previous seismic investigations of the TAMs have been primarily focused on the central portion of the mountain range, in the vicinity of Ross Island. For example, data from the Transantarctic Mountains Seismic Experiment (TAMSEIS; Figure 1), which operated between 2000 and 2003, have been analyzed with a variety of techniques to examine the crustal and upper mantle structure beneath this area. However, even using the same data set, different TAMSEIS studies came to different conclusions [e.g., *Lawrence et al.*, 2006a; *Hansen et al.*, 2009]. A main point of contention between these studies, and between suggested origin models, is whether or not the TAMs are underlain by thick crust (i.e., a crustal root) and whether distributed flexural isostatic compensation plays a role in supporting the TAMs uplift and elevation. Further, along-strike investigations of the crustal structure beneath the TAMs and the WSB are needed to constrain their corresponding origin mechanisms and to assess how these features relate to the overall tectonic history of Antarctica.
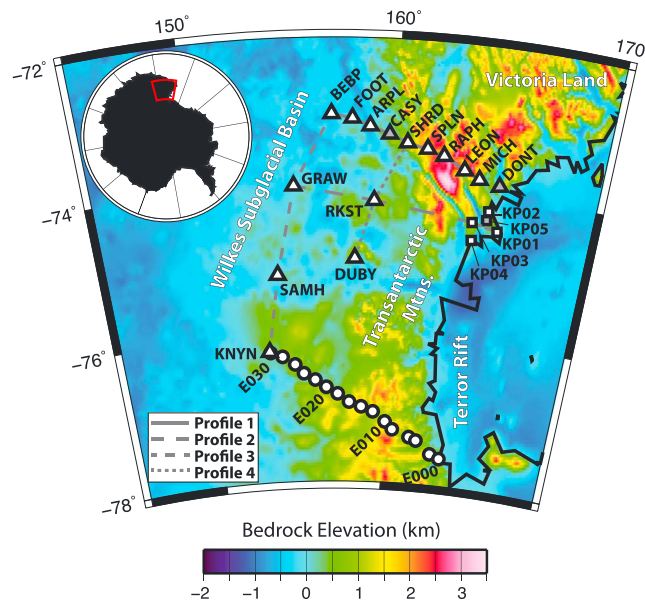
Figure 1. Map of the TAMNNET (triangles) and KOPRI (squares) stations. For reference, stations from the east-west TAMSEIS array are also shown (circles). Shapes with grey centers denote stations that did not produce a high signal-to-noise ratio SRF stack. Bedrock elevations are from the BEDMAP2 model [*Fretwell et al.*, 2013]. Four profiles are highlighted by the grey lines: Profile 1, which extends from station MICH to station BEBP along the main TAMNNET transect; Profile 2, which extends between stations KP01 and GRAW; Profile 3, which extends between stations BEBP and KNYN; and Profile 4, which extends between stations SHRD and DUBY.

Often, *P* wave receiver functions (PRFs) are employed in seismic studies to estimate the crustal structure by modeling *P*-to-*S* wave (Ps) conversions from the crust-mantle interface (Moho) [*Langston*, 1977, 1979; *Ammon et al.*, 1990; *Ammon*, 1991; *Zhu and Kanamori*, 2000]. However, when a low-velocity surface layer, such as ice, is present, the Moho Ps phase can be masked by reverberations and noise within that slow layer (Figure 2) [*Zelt and Ellis*, 1999; *Juliá et al.*, 2004; *Kumar et al.*, 2005]. In such cases, *S* wave receiver functions (SRFs), which instead model *S*-to-*P* wave (Sp) conversions, can be advantageous. Timing differences between the converted phases of interest and reverberations in the slow surface layer make SRFs well suited to imaging deeper structure [*Farra and Vinnik*, 2000; *Li et al.*, 2004; *Hansen et al.*, 2009].

In this study, we use the SRF approach to estimate the crustal structure beneath the TAMs and the WSB to expand the investigation of their origins. Data for our analysis are provided by a new seismic array, the Transantarctic Mountains Northern Network (TAMNNET; Figure 1) [*Hansen et al.*, 2015], as well as from a five-station array operated by the Korea Polar Research Institute (KOPRI) [*Park et al.*, 2014]. These two networks provide seismic coverage of a previously unexplored portion of the northern TAMs and WSB. The timing of Moho Sp conversions identified on our SRFs is combined with Rayleigh wave phase velocities that have also been modeled using the new TAMNNET data [*Graw et al.*, 2014]. Our crustal estimates beneath the northern TAMs will help elucidate whether a crustal root is present beneath the mountain range and whether there are any along-strike variations of the crustal structure between the central and northern TAMs. Combined with previous results from TAMSEIS, this study provides a cohesive set of evidence that constrains origin models for the TAMs and the WSB.

2. Geologic Constraints and Previous Studies

2.1. Tectonic History of the TAMs

The geologic history of the TAMs is inferred from various outcrops, particularly in the McMurdo Dry Valleys region. Precambrian igneous and metamorphic rocks from the Beardmore Orogeny [*ten Brink et al.*, 1997] are unconformably overlain by Cambrian metasedimentary rocks. Cambrian-Ordovician syntectonic to posttectonic granites from the Ross Orogeny, which were emplaced in the overriding plate of a subduction zone that paralleled the present-day TAMs [*Federico et al.*, 2009], intrude the metasedimentary strata. During the Ordovician-Devonian, a distinct horizontal erosional surface called the Kukri Peneplain developed [*Fitzgerald et al.*, 1986], which is overlain by the Devonian to Triassic sedimentary Beacon Supergroup [*Fitzgerald et al.*, 1986; *Fitzgerald*, 2002; *Bialas et al.*, 2007]. Jurassic dolerite dikes and sills intrude both the Beacon Supergroup and the basement, and the sills are generally parallel to the peneplain [*Fitzgerald et al.*, 1986].

The peneplain, sills, and the flat-lying Beacon sediments have been used as indicators of post-Jurassic tectonic movement. For example, the Kukri Peneplain was buried up to ~4 km between 180 Ma and at least
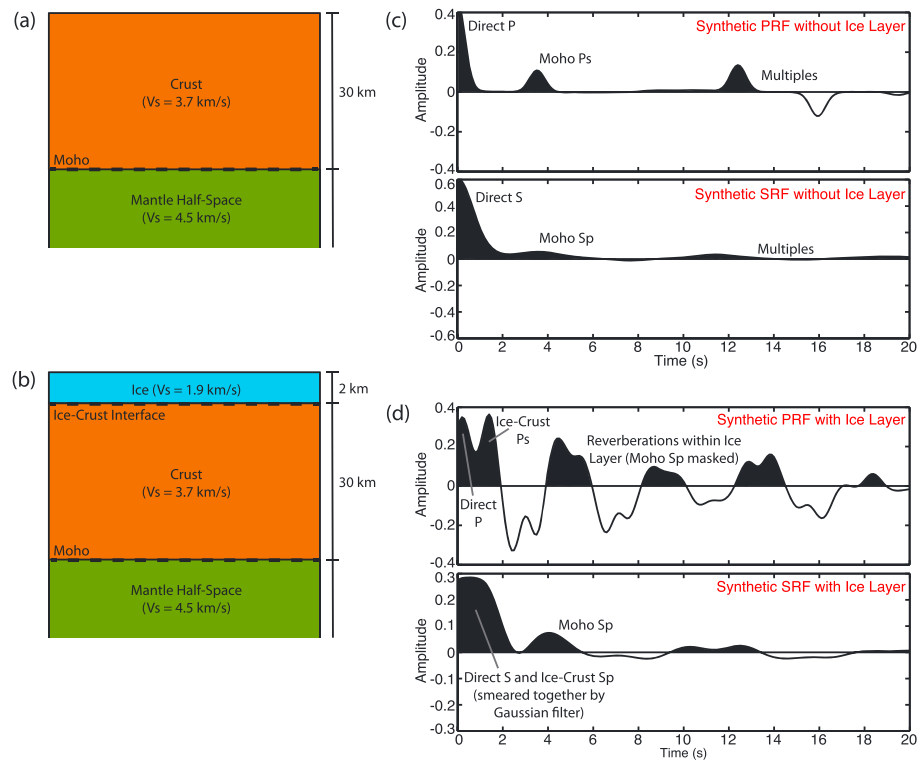
Figure 2. Synthetic receiver function examples. (a) Simple input model with 30 km thick crust overlying a mantle half-space. The shear velocity (V_s) of each layer is indicated. (b) Same as Figure 2a but with a 2 km thick ice layer now included at the surface. (c) Synthetic PRF (top) and SRF (bottom) stacks corresponding to the input model shown in Figure 2a. The Moho conversion is observed on both synthetic receiver function stacks, though the amplitude of the Sp conversion is smaller than that of the Ps conversion. (d) Synthetic PRF (top) and SRF (bottom) stacks corresponding to the input model shown in Figure 2b. The addition of the ice layer causes numerous reverberations, masking the conversion from the Moho on the PRF. However, on the SRF, the Moho conversion is clearly observed. Also note that the direct *S* wave and the Sp conversion from the ice-crust interface are smeared together by the Gaussian filter used.

80 Ma [*Lisker and Laufer*, 2013]. Today, the peneplain is nearly horizontal, with a gentle dip to the west, and can be found at elevations 500–4000 m above sea level [*Fitzgerald et al.*, 1986; *Stern and ten Brink*, 1989]. Neither the peneplain nor the Beacon sediments show evidence of folding or reverse faulting associated with a collisional origin.

The study area is also situated just to the south of Victoria Land (Figure 1). While the Beacon Supergroup and the Jurassic-aged dolerites extend into this area, a series of NW-SE trending strike-slip faults separate these geologic units from three other distinct terrains [*Storti et al.*, 2008]. Cambrian-Ordovician granitic rocks of the Wilson Terrain, including the Granite Harbor Intrusive complex, provide additional evidence of the Early Paleozoic Ross Orogeny [*Stump*, 1992; *Armienti et al.*, 1990]. To the north-northeast, the Bowers Terrain and the Robertson Bay Terrain consist of low-grade metavolcanic and slightly metamorphosed clastic rocks, respectively [*Weaver et al.*, 1984; *Burrett and Findlay*, 1984; *Rossetti et al.*, 2006]. It has been suggested that the Bowers Terrain marks a major crustal boundary and that rocks in northern Victoria Land are unique compared to those seen in the TAMs [*Stump et al.*, 1983]. Cenozoic volcanic rocks of the Meander Intrusive Group and the McMurdo Volcanic Group trend roughly N-S through Victoria Land, primarily concentrated along the coast, and several active volcanoes are part of this magmatic belt [*Kyle and Cole*, 1974; *LaMasurier*, 1990; *Storti et al.*, 2008].

2.2. Proposed Uplift Models for the TAMs

Numerous models have been proposed to explain the TAMs uplift (see supporting information Figure S1). One of the earliest models was from *Fitzgerald et al.* [1986], who examined apatite fission track data in relation to regional geologic observations. They suggested that strain resulting from the formation of the Ross

Embayment was not equally partitioned between the crust and the subcrustal lithosphere, leading to isostatic uplift of the TAMs. This model also considers the contribution of additional buoyancy from magmatic underplating following the deposition of the Beacon Supergroup. Roughly a decade later, *Stern and ten Brink* [1989] and *ten Brink et al.* [1997, and references therein] employed elastic modeling, high-resolution subglacial topography from seismic and radar surveys, and gravity measurements to suggest an alternative model for the TAMs, where the mountain range resulted from broad flexure of the East Antarctic lithosphere along its western, rifted edge. In their model, lateral heat conduction from hotter mantle beneath West Antarctica provided a thermal load that aided in the uplift. They also contend that isostatic rebound following erosion of the TAMs and adjacent outlet glaciers contributed to the uplift.

More recently, *Studinger et al.* [2004] and *Karner et al.* [2005] modeled aerogeophysical and shipboard gravity data, respectively, to assess the TAMs uplift. Both of these studies suggested that the TAMs developed as the result of rift flank uplift and climate-induced erosional unloading. Their models do not include a thermal load beneath the TAMs but instead require a crustal root to help provide isostatic buoyancy. Other studies have also advocated for a crustal root beneath the mountain range, possibly as a remnant of extensional collapse of a region of thickened crust in western Antarctica [*Bialas et al.*, 2007; *Bialas*, 2009; *Huerta and Harry*, 2007; *Fitzgerald et al.*, 2007; *van Wijk et al.*, 2008]. Alternatively, *Lawrence et al.* [2006a] used their analysis of PRFs and Rayleigh wave phase velocities to propose a hybrid model that includes local crustal isostasy, thermal loading, erosion unloading, and a flexural response associated with rift flank uplift.

Crustal thickness beneath the central TAMs, in the vicinity of Ross Island, has been investigated in several studies. *Bannister et al.* [2003] used PRF analysis to demonstrate that the crust thickens from 18–20 km beneath the Ross Sea coastline, immediately adjacent to the TAMs, to 36–40 km beneath the TAMs. *Lawrence et al.* [2006a] found similar results, with a maximum crustal thickness of 40 ± 2 km beneath the crest of the TAMs. The *Lawrence et al.* [2006a] study also indicated that the average crustal thickness beneath East Antarctica is about 35 km, suggesting that the TAMs are underlain by a 5 ± 2 km thick crustal root which helps provide isostatic support to the mountain range. In contrast, *Hansen et al.* [2009] modeled SRFs and Rayleigh wave group velocities and found 40 ± 3 km thick crust beneath both the TAMs and East Antarctica, providing little to no evidence of a crustal root beneath the mountain range and instead suggesting that crustal buoyancy does not significantly contribute to the TAMs uplift. All of these studies examined only a small geographic portion of the TAMs, and additional characterization of the crustal structure along the mountain front is necessary to more accurately assess competing origin models.

2.3. Tectonic History and Proposed Models for the WSB

The WSB is marked by a long-wavelength, down-warped region extending from the Oates Coast to southern Victoria Land, parallel to the inland side of the TAMs (Figure 1). The width of the WSB changes from ~600 km at its north end to ~100 km at about 84°S latitude [*Ferraccioli et al.*, 2001]. Similar to the TAMs, the structure and formation of the WSB remains elusive. Models of gravity [*Drewry*, 1976; *Ferraccioli et al.*, 2001] and magnetic [*Ferraccioli et al.*, 2001, 2009] anomalies have led some to suggest that the WSB may have formed as a result of rifting. These studies suggest that the basin is underlain by thin, rifted continental crust (31 ± 2 km thick) covered by several kilometers of low-density sedimentary fill. Other studies based on aerogeophysical data, such as *Studinger et al.* [2004], support the idea of thinned crust but argue that the location of the basin is controlled by preexisting structure between the TAMs and the Belgica Subglacial Highlands further inland and that the maximum possible sediment thickness within the basin is less than 1 km. Alternatively, elastic [*Stern and ten Brink*, 1989; *ten Brink and Stern*, 1992] and numerical models [*van Wijk et al.*, 2008] have instead suggested that the WSB has a flexural origin. In these models, the basin is an "outer low" linked to the uplift of the TAMs and to the flexural rigidity of the East Antarctic lithosphere. The flexural and numerical models predict crustal thickening, up to about 45 km, beneath the WSB.

Analysis of the TAMSEIS data has provided the few available seismic constraints on the WSB. Again, using a joint PRF and Rayleigh wave phase velocity inversion, *Lawrence et al.* [2006a] indicate that thick (>1 km), shallow low-velocity layers are present in the basin. Additionally, they suggest that the underlying crust may be somewhat thinner than that observed beneath East Antarctica (35 ± 3 km), but this observation is at the limit of their resolution. *Pyle et al.* [2010], who imaged the region with ambient noise tomography, concluded that while low velocities are observed beneath the WSB, the sediment thickness must be limited to less than 2 km. *Hansen et al.* [2009] modeled the crustal structure beneath the TAMSEIS array, including a small portion of the

WSB, and observed comparable crustal thickness beneath the basin to that beneath the rest of East Antarctica (40 ± 3 km). Given the limited geographic sampling of these studies, additional investigation of the WSB is required to more fully characterize the crustal structure and to interpret the origin of the basin.

3. Data and Methodology

To further investigate the origins of the TAMs and the WSB, seismic data from the new TAMNNET deployment are used [*Hansen et al.*, 2015]. TAMNNET was installed in November–December 2012, and two years of continuous data are incorporated into this study. Ten TAMNNET stations were deployed in a linear transect across the TAMs, starting near the coast ~50 km north of Mount Melbourne and extending into the WSB (Figure 1). One station (KNYN) reoccupies the former location of previously deployed station E030 from the TAMSEIS array. The four remaining TAMNNET stations were deployed to provide coverage of the area between the current TAMNNET transect and the former east-west TAMSEIS transect (Figure 1). Additional data are provided by five KOPRI-operated stations, which were installed during the 2011 and 2012 Antarctic field seasons [*Park et al.*, 2014]. The KOPRI stations are positioned on and around Mount Melbourne in Terra Nova Bay and are all located within 40 km of the coast (Figure 1).

3.1. SRF Analysis

SRFs were generated using the approach outlined by *Hansen et al.* [2009, 2010]. Earthquakes were limited to magnitudes of 5.5 or larger, depths less than 200 km, and distances between 60 and 80°, which optimizes the S wave signal-to-noise ratio and prevents interference from other teleseismic phases [*Wilson et al.*, 2006]. In total, 272 earthquakes met this criteria. After rotating the waveforms from north-east-vertical to radial-transverse-vertical orientation, the data were visually inspected to pick the S wave onset. The iterative time domain method from *Ligorria and Ammon* [1999] was then used to create the SRFs by deconvolving the radial component from the corresponding vertical component. Since the Sp conversion from the Moho arrives before the direct S wave, the waveforms must be flipped in time prior to deconvolution. The frequency content of the SRF is controlled by the width factor of the Gaussian filter, a [*Ligorria and Ammon*, 1999], which is used to remove high-frequency noise from the receiver function. Several values of a were examined, but the best and most consistent results were obtained using an a of 1.0. To improve the signal-to-noise ratio, individual SRFs for each station were stacked, and each stack contains between 20 and 47 records (Figure 3). Our data set is dominated by events arriving from the northwest, and at crust-mantle depths, the corresponding Sp conversion points lie somewhat inland of each station (see supporting information Figure S2). Therefore, moving from east to west, the individual station stacks display the inland trend of the crustal structure. It should be noted that stations DONT, CASY, and KP05 did not record enough high signal-to-noise ratio data to produce quality SRF stacks; therefore, these stations are not used for further analysis.

Comprehensive station stacks along four different profiles are shown in Figure 3. On each stack, the initial arrival near 0 s is the direct S phase combined with the Sp conversion from the ice-crust interface. The a value used in our analysis produces a fairly wide filter that smoothes these signals together (Figure 2) [*Hansen et al.*, 2009]. The second arrival observed is the Sp conversion from the Moho (Figure 3), and the arrival time of this phase varies between 2.30 s (station KP02) and 6.65 s (station SAMH), indicating the variability in the crustal structure. 2σ bootstrap error bounds for each stack were determined using 100 randomly resampled sets of the data, following the method of *Efron and Tibshirani* [1991], and these provide further constraints on the SRF uncertainty. As shown on Figure 3, all Moho Sp conversions are well resolved with high signal-to-noise ratios above the bootstrap error limits.

3.2. Estimating Ice Structure

To model the subsurface structure beneath each station, the corresponding ice thickness must also be determined, and PRFs were employed for this purpose. The PRF approach used is almost identical to the SRF method described in section 3.1. However, for the PRFs, earthquake magnitudes and distances were restricted to 5.5 or larger and 30–90°, respectively. Also, given the higher frequency content of P arrivals, the computed PRFs for the TAMNNET stations were generated using an a of 2.1 [*Ligorria and Ammon*, 1999]. All KOPRI stations were deployed on rock, so there is no corresponding ice thickness for these stations.
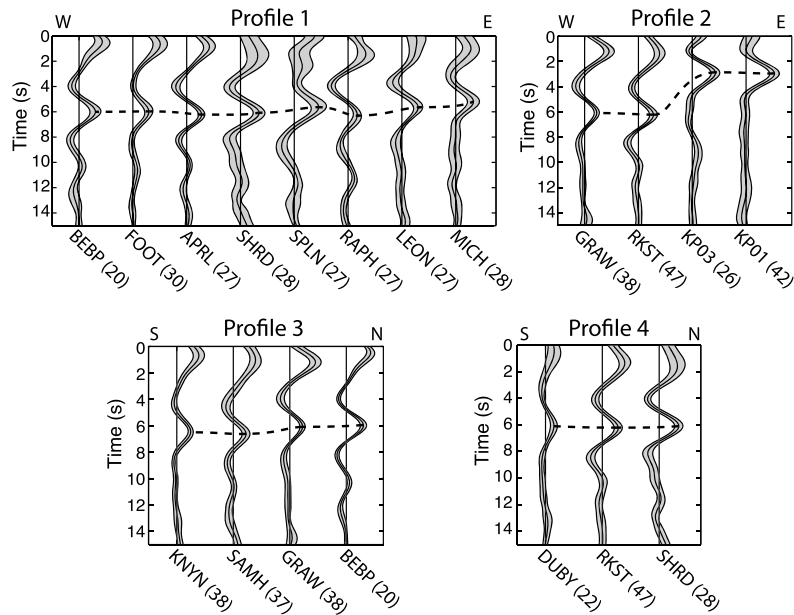
Figure 3. Stacked SRFs along each of the four profiles highlighted in Figure 1. The black dashed line denotes the Moho Sp conversion beneath each station, and grey shaded regions denote the 2σ bootstrap error bounds. Numbers in parentheses after station names indicate the number of individual receiver functions contributing to that station stack. Note that these plots are not to scale laterally.

The stacked PRFs are dominated by multiples from the Ps conversion at the ice-crust boundary (Figure 4), and these can be modeled to determine the ice thickness. However, in order to do so, the velocity of the ice must also be estimated, and additional data can be employed to further constrain this parameter. More specifically, if an estimate of the ice thickness is available, such as from ice-penetrating radar, we can use that thickness measurement to estimate the ice velocity. The availability of radar data over our study area is limited, but the closest radar-determined ice thickness measurement was 3.5 km from station GRAW [*Blankenship et al.*, 2013], where the ice is 2.1 km thick. Synthetic PRFs were generated for this station, and the S wave velocity (V_s) of the ice layer needed to be 1.9 km/s in order to match the radar-determined ice thickness. This is a reasonable value given the accepted range of ice sheet V_s (1.5–2.0 km/s) [e.g., *Kim et al.*, 2007; *Hansen et al.*, 2010]. The ice V_s was then held fixed at this value, and synthetic PRFs were generated for the other stations to determine their corresponding ice thicknesses. Ice thickness estimates from the PRFs were also compared to those from the BEDMAP2 model, which was generated from a variety of data sources including radar surveys, gravity measurements, and seismic soundings throughout Antarctica [*Fretwell et al.*, 2013]. As shown in Table 1, there is generally good agreement between our ice thickness estimates and those from BEDMAP2.

It should be noted that the PRFs for several stations (MICH, RAPH, SPLN, and SHRD) indicated a very thin ice layer, and the corresponding Ps conversion could only be modeled to within 0.5 km. Comparing to BEDMAP2 [*Fretwell et al.*, 2013], these four stations have ice thicknesses ranging from 0.10 to 0.45 km, and it is difficult to
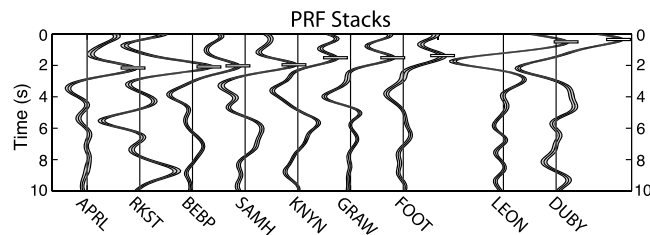

Figure 4. Stacked PRF examples. The first Ps multiple from the ice-crust interface is marked with a tick on each receiver function, and the associated timing was used to model the ice thickness beneath each station. Similar to Figure 3, the grey shaded regions denote the 2σ bootstrap error bounds for each stack. Stations do not lie on the same profile but are rather ordered from left to right by decreasing ice thickness.

Table 1. Summary of Ice Thickness Estimates From the PRF Analysis[a]

Station	Latitude (°)	Longitude (°)	Ice Thickness From PRFs (km)	Ice Thickness From BEDMAP2 (km)
KP01	−74.4866	165.2897	0.00	0.00
KP02	−74.2319	164.7334	0.00	0.00
KP03	−74.3995	163.9708	0.00	0.00
KP04	−74.6448	164.0360	0.00	0.00
MICH	−73.8171	164.0998	<0.50	0.30
LEON	−73.7134	163.3278	1.30	1.15
RAPH	−73.5473	162.2885	<0.50	0.10
SPLN	−73.4662	161.4712	<0.50	0.45
SHRD	−73.3989	160.4988	<0.50	0.20
APRL	−73.1949	158.7034	2.90	2.85
FOOT	−73.0934	157.8534	2.00	2.40
BEBP	−73.0325	156.8690	2.75	2.90
RKST	−74.2011	159.0018	2.75	1.70
DUBY	−74.9853	158.0773	1.15	0.90
SAMH	−75.2030	153.9968	2.60	2.00
GRAW	−74.0042	154.9887	2.10	2.50
KNYN	−76.2374	153.3270	2.15	1.85

[a]Ice thicknesses from BEDMAP2 [*Fretwell et al.*, 2013] are also shown for comparison.

resolve layers this thin with PRFs. Therefore, for these four TAMNNET stations, the ice thickness was taken directly from BEDMAP2 [*Fretwell et al.*, 2013].

3.3. Estimating Crustal Structure

To estimate the crustal structure beneath each station, a grid search method similar to *Hansen et al.* [2009, 2010] was used. First, a variety of velocity models were created for each station, where the models include an ice layer (where appropriate), a two-layer crust, and an upper mantle half-space. As in the PRF analysis, the ice V_s was fixed at 1.9 km/s. Ice density and Poisson's ratio were also fixed at 0.92 g/cm^3 and 0.33, respectively, and the ice thickness was based on the PRF results or BEDMAP2 [*Fretwell et al.*, 2013], as discussed previously. Each model also had a fixed mantle velocity of 4.5 km/s and fixed Poisson's ratios for the crust and mantle of 0.25 and 0.28, respectively. Similar to the approach of *Last et al.* [1997], the velocities in the crustal layers were averaged by slowness to equal a mean crustal shear velocity ($\overline{V_s}$), which was allowed to vary from 2.9 to 3.9 km/s in 0.05 km/s increments. Similarly, the crustal thickness was varied from 10 to 60 km in 1 km increments.

For each examined velocity model, a synthetic dispersion curve was calculated at periods between 18 and 30 s. These calculated dispersion values were then compared to smoothed dispersion curves from Rayleigh wave phase velocity analysis that was also conducted with the TAMNNET data. Seismograms from 877 events were sampled at different periods ranging from 18 to 103 s, and the two-plane wave method of *Forsyth and Li* [2005] was used to generate phase velocity maps for the fundamental mode Rayleigh wave at each period [*Graw et al.*, 2014]. We focus our examination on the shorter periods because they are the most sensitive to crustal and upper mantle structure. To be conservative, the uncertainty estimates provided by *Graw et al.* [2014] were multiplied by 1.5, and models that match the dispersion data within an error of ±0.09 km/s were retained. Each retained model was then further examined by comparing its predicted Moho Sp conversion time to that observed on the stacked SRF (Figure 3). For a given station, the depth and distance of each event contributing to the SRF stack was used to determine an average ray parameter, which was, in turn, used to compute the vertical slowness for each layer in the velocity model and to ultimately predict the Sp conversion timing. The bootstrap error bounds (Figures 3 and 5a, inset) indicate that the Moho Sp phases have a corresponding uncertainty that averages ±0.4 s; therefore, predicted Sp times that match the observed SRF timing within this uncertainty were accepted [*Hansen et al.*, 2009, 2010]. The suite of models that fit both the dispersion and SRF data within error were used to determine the average crustal thickness and $\overline{V_s}$ beneath a given station. An example of this data modeling is shown in Figure 5, and additional examples are shown in supporting information Figure S3. Our crustal estimates are summarized in Table 2.
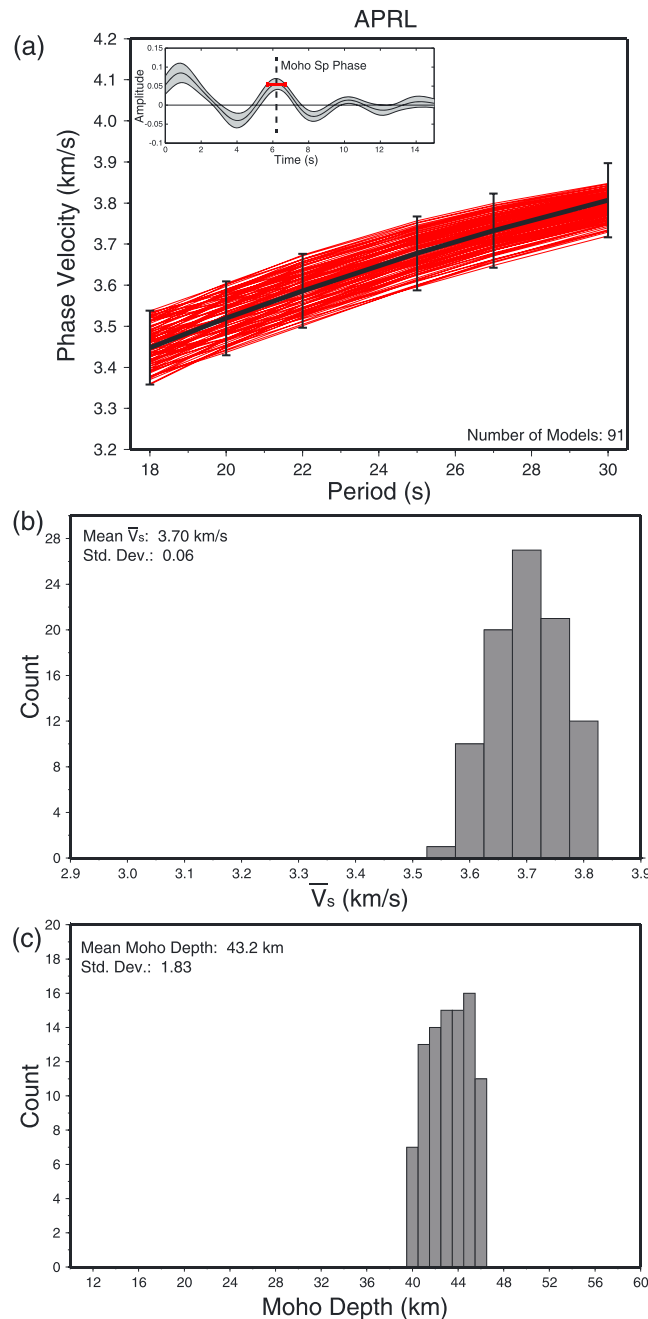
Figure 5. Data modeling and grid search results, using station APRL as an example. (a) Thin, red lines show the predicted Rayleigh wave phase velocity dispersion curves for models that fit both the observed dispersion data (black line with error bars) [*Graw et al.*, 2014] and the Moho Sp conversion time within error, as described in the text. The inset on the upper left highlights the SRF stack for this station, illustrating how the 2σ bootstrap error bounds constrain the Moho Sp timing uncertainty. (b) The range of mean crustal shear velocities ($\overline{V}_s$) encompassed by the "fit" models from Figure 5a. (c) The range of Moho depths encompassed by the fit models from Figure 5a. Note that the Moho depths here include the thickness of the ice layer.

3.4. Assessing Additional Uncertainty

As described in the previous section, the range of models that match both the dispersion data and the SRF timing in the grid search provides some estimate of uncertainty for our results. Across all stations, the standard deviations associated with the average crustal thickness and $\overline{V}_s$ are 1.7 km and 0.06 km/s, respectively. However, uncertainty can also arise from the fixed parameters used in the grid search. To account for this, the ice thickness, ice velocity, and crustal Poisson's ratio were varied within reasonable limits to assess the corresponding model differences. As described in section 3.2, the ice thickness for most stations was obtained from our PRF analysis. Comparing these ice thickness values to those from BEDMAP2 (Table 1) [*Fretwell et al.*, 2013], the average ice thickness differed by ~0.2 km. Previous studies indicate that while ice V_s values can vary, they generally fall between 1.5 and 2.0 km/s [*Kim et al.*, 2007]. In Antarctica, crustal Poisson's ratios have been estimated between 0.24 and 0.27 [*Finotello et al.*, 2011]. By setting the ice V_s to 2.0 km/s, decreasing the ice thickness by 0.2 km, and setting the crustal Poisson's ratio to 0.24, the maximum crustal thickness for a given station associated with these parameter uncertainties can be determined. Similarly, the minimum crustal thickness estimate can be found by setting the ice V_s to 1.5 km/s, increasing the ice thickness by 0.2 km, and setting the crustal Poisson's ratio to 0.27. Using these parameter variations in the grid search, the average crustal thickness and $\overline{V}_s$ uncertainties are ±2 km and ±0.04 km/s, respectively. Combining these uncertainties with the standard deviations from the original grid search results, it is estimated that the crustal thickness is resolved to within ±4 km and that the $\overline{V}_s$ is resolved to within ±0.1 km/s.

Table 2. Summary of Mean Crustal Thickness and Mean Crustal Shear Velocity ($\overline{V}_s$) at Each Station, Along With the Associated Standard Deviations, Determined Using our Grid Search Technique

Station	Mean Crustal Thickness (km)	Standard Deviation of Mean Crustal Thickness	$\overline{V}_s$ (km/s)	Standard Deviation of $\overline{V}_s$
KP01	20.8	2.07	3.28	0.14
KP02	16.7	0.87	3.03	0.09
KP03	21.0	1.22	3.04	0.08
KP04	16.9	1.59	3.13	0.11
MICH	37.6	1.98	3.57	0.07
LEON	39.0	1.83	3.63	0.06
RAPH	46.0	1.98	3.70	0.05
SPLN	40.7	1.90	3.65	0.06
SHRD	44.6	1.76	3.72	0.04
APRL	40.3	1.83	3.70	0.06
FOOT	40.0	1.87	3.67	0.06
BEBP	38.5	1.70	3.70	0.04
RKST	40.2	1.41	3.87	0.05
DUBY	42.2	1.03	3.88	0.03
SAMH	43.9	1.94	3.67	0.05
GRAW	41.5	1.87	3.83	0.06
KNYN	43.1	1.83	3.57	0.05

4. Results

Figure 6 illustrates our crustal thickness estimates, in relation to bedrock and surface topography, along four profiles through the study area. Along the main TAMNNET transect (Profile 1), the Moho depth increases from 38 ± 4 km beneath station MICH to 46 ± 4 km beneath station RAPH, which is the highest elevation station in the array (3052 m). Average crustal thickness beneath the TAMs is ~44 km, but the Moho then shallows
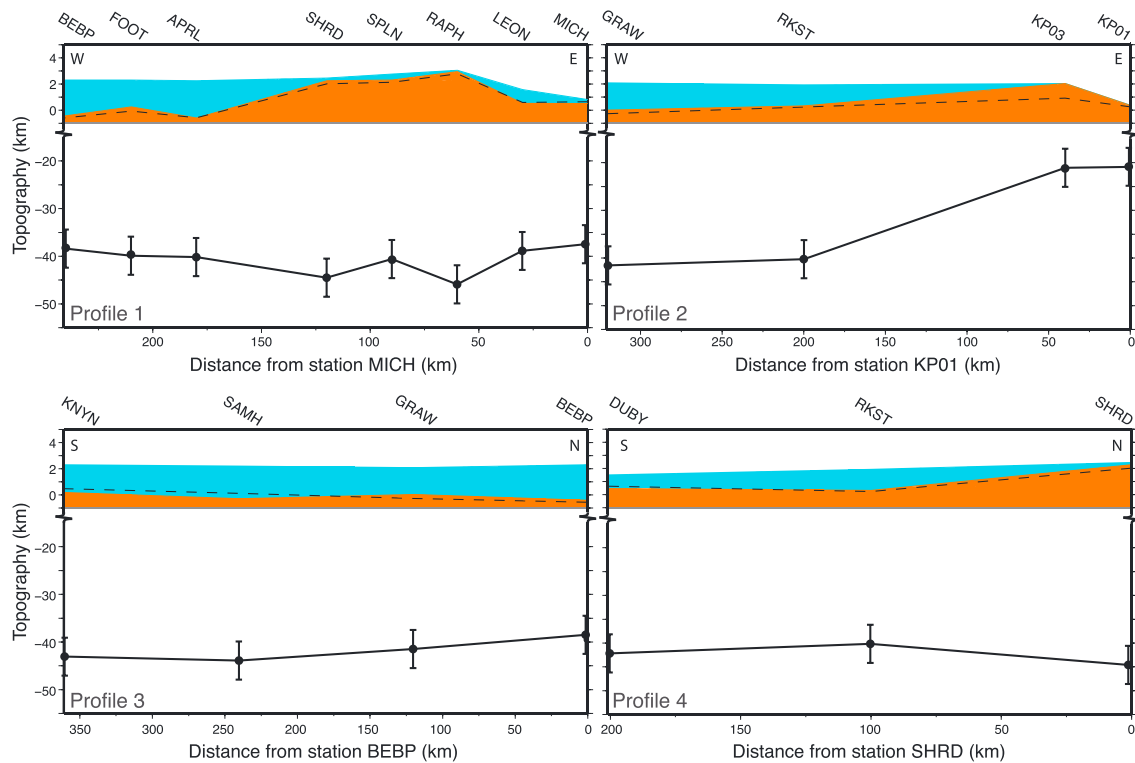

Figure 6. Moho variations along the four profiles highlighted in Figure 1. For all plots, the blue shaded area indicates the ice layer, and the tan shaded area indicates the bedrock topography. Bedrock elevations were determined by subtracting the thickness of the ice layer from the corresponding station elevation. The black dashed line shows bedrock topography from BEDMAP2 [*Fretwell et al.*, 2013] for comparison. The Moho depth estimates are plotted as black dots with ±4 km error bars, as described in the text. Note the change of scale on the vertical axis of each plot.
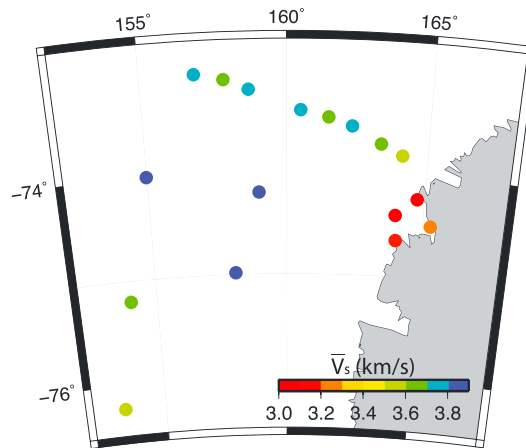
Figure 7. Average crustal shear velocities ($\overline{V}_s$) beneath the TAMNNET and KOPRI stations, plotted as circles where the colors correspond to velocity (km/s).

somewhat to an average depth of ~41 km beneath the WSB. Along parallel Profile 2, crustal thickness beneath the coastal KOPRI stations averages ~20 km, with the Moho depth again increasing inland to ~41 km depth. Profiles 3 and 4 illustrate the crustal thickness both behind and along the TAMs front, respectively. Along the mountain front, we again see thick crust (~45 km) beneath the TAMNNET transect; however, the crust thins to ~41 km to the south, moving toward the east-west TAMSEIS array. Behind the mountain front, along the eastern WSB, we observe fairly uniform crustal thickness (~41 km) along the entire profile.

Generally, our crustal thickness estimates well match those from previous studies that examined the central portion of the TAMs near Ross Island. For instance, using multichannel seismic reflection and refraction data, *ten Brink et al*. [1993] suggested that the crust is ~30–35 km thick ~40 km inland from the Ross Sea. *Bannister et al*. [2003] examined PRFs and reported ~20 km thick crust ~30 km inland from the coast and 36–40 km thick crust ~85 km inland. *Finotello et al*. [2011] and H. J. Yoo et al. (Crustal and upper mantle structure beneath Mt. Melbourne, Antarctica: Implications for partial melting, submitted to *Journal of Geophysical Research*, 2015) also used PRFs to examine coastal TAMSEIS and KOPRI stations, respectively, finding results similar to those reported here. *Hansen et al*. [2009] employed an SRF methodology similar to that used in the current study to examine TAMSEIS data. They found ~25 km thick crust near the Ross Sea coast and ~44 km thick crust beneath the inland end of the east-west TAMSEIS profile (Figure 1). As stated previously, TAMNNET station KNYN reoccupies the site of TAMSEIS station E030, and our crustal thickness estimate of 43 ± 4 km at this site agrees with the 44 ± 3 km estimate from *Hansen et al*. [2009].

Our $\overline{V}_s$ results are illustrated in Figure 7. Generally, lower $\overline{V}_s$ values are observed near the coast, with higher $\overline{V}_s$ values seen further inland. All the KOPRI stations have $\overline{V}_s$ values of ~3.0–3.3 km/s. Along the TAMNNET transect, $\overline{V}_s$ values range between ~3.6 and 3.7 km/s. Several stations along the TAMs front and within the WSB (RKST, DUBY, and GRAW) show faster $\overline{V}_s$ of ~3.8–3.9 km/s, but stations further south (SAMH and KNYN) have average crustal velocities similar to those seen beneath the TAMNNET transect (~3.6–3.7 km/s).

Similar to our crustal thickness estimates, our $\overline{V}_s$ results are comparable to those from previous studies. The midcrustal shear velocities (3.4–3.8 km/s) from *Bannister et al*. [2003] and the $\overline{V}_s$ estimates (~3.6–3.7 km/s) from *Hansen et al*. [2009] are consistent with our findings. *Pyle et al*. [2010] used ambient noise tomography to generate shear velocity models down to 45 km depth beneath the TAMs, the Ross Sea, and the WSB. While their models are more detailed than the $\overline{V}_s$ determined in the current study, the crustal velocities beneath the TAMs and the WSB range between 3.3 and 3.9 km/s [*Pyle et al*., 2010], similar to our estimates. H. J. Yoo et al. (submitted manuscript, 2015), who examined the structure beneath the KOPRI stations, reported an average crustal V_s of ~3.4 km/s and suggested the KOPRI stations are underlain by crust with a bulk intermediate to felsic composition.

5. Discussion

5.1. Crustal Thickness and Isostatic Compensation

While our findings are similar to those of *Hansen et al*. [2009], an interesting difference is observed. Both the east-west TAMSEIS transect and the TAMNNET transect have similar lengths and cross the TAMs approximately parallel to one another (Figure 1), and both display a general crustal thickening from the Ross Sea coast inland. However, the maximum surface elevation on the TAMNNET profile is ~1 km higher than that on the TAMSEIS profile. Beneath the northern TAMs, the thickest crust is 46 km ± 4 km, which is somewhat thicker than the 41 ± 3 km reported beneath TAMSEIS [*Hansen et al*., 2009]. While the uncertainty estimates

for these measurements slightly overlap, the difference in crustal thickness between these two profiles may explain the difference in their corresponding surface topography. It should be noted that while potentially thicker crust is observed along the TAMNNET profile, an increased Moho depth does not appear to trend along-strike of the TAMs. That is, thicker crust is not observed beneath the TAMs on Profile 2, which is situated between the TAMNNET and TAMSEIS transects, and instead, the crustal thickness is more comparable to that found by *Hansen et al*. [2009].

An examination of the surface topography along the TAMNNET and TAMSEIS transects is explored to assess the crustal variability. The following equation is used to roughly estimate the additional crustal root expected for an additional ~1 km of elevation:

$$T = (\rho_c * h)/(\rho_m - \rho_c)$$

In this equation, T is the thickness of the crustal root, h is the height of the isostatic topography, and ρ_c and ρ_m are the densities of the crust and mantle, respectively [*Turcotte and Schubert*, 2002]. Approximating ρ_c and ρ_m as 2.8 and 3.3 g/cm^3, a topographic change of 1 km is associated with a 5.6 km root. This is a close match to the difference in crustal thickness observed beneath the TAMSEIS (~41 km) and TAMNNET (~46 km) transects.

The above equation can also be used to estimate the total crustal thickness that would be required to support the topography along the TAMNNET transect in local isostatic equilibrium. For context, we will assume that the crust behind the TAMs front is already isostatically compensated since there is no significant bedrock topography along Profile 3 (Figure 6). The average crustal thickness of ~41 km beneath this profile is used as a reference thickness. The highest elevations in our study area are found near station RAPH, and using the BEDMAP2 model [*Fretwell et al*., 2013], the mean elevation in the vicinity of this station (within 1 km lateral distance) is ~2800 m or, in other words, an extra 2.8 km of elevation compared to Profile 3. Using this value in the previous equation, a total crustal thickness of ~57 km would be needed to isostatically support these high elevations. The reference elevation along Profile 3 could also be adjusted by the rock equivalent thickness of the overlying ice mass. Again, assuming an ice density of 0.92 g/cm^3, the average ice thickness of 2.4 km along Profile 3 is equivalent to about 789 m of 2800 g/cm^3 density rock, ultimately leading to an "effective" elevation difference of about 2 km, which would require a total crustal thickness of ~52 km for isostatic support. In either case, the total crustal thickness required is well outside the observed crustal thickness and uncertainty estimate of 46 ± 4 km beneath station RAPH, demonstrating that the TAMs high topography is not in isostatic equilibrium.

5.2. Assessment of TAMs Uplift Models

The lack of a crustal root thick enough to fully isostatically compensate the observed TAMs elevations is clear. However, the uncertainty associated with our crustal thickness estimates makes it difficult to assess if a small (3–5 km) root is present beneath the northern TAMs, and the somewhat thicker crust beneath Profile 1 (Figure 6) indicates that this may be a possibility. *Studinger et al*. [2004], *Lawrence et al*. [2006a], and *Bialas et al*. [2007] suggested that a 4–5 km thick crustal root may be present beneath the mountain range. *Studinger et al*. [2004] used this small root to model Airy isostasy, though they acknowledged that such a root would not sufficiently support the observed elevations and suggested that erosional unloading may also have contributed to TAMs uplift. Both *Studinger et al*. [2004] and *Bialas et al*. [2007] suggested that such a root may have resulted from the collapse of a plateau of thickened crust and that erosional denudation shrank the root, leading to higher elevations in the TAMs. *Lawrence et al*. [2006a] also include a small root in their TAMs uplift model, which combines isostatic compensation, thermal loading, erosional unloading, and flexure to support the mountain range.

If a small (4–5 km) root does play an important role in supporting the TAMs, it should be a continuous feature along-strike. However, as shown in this study, that does not seem to be the case. The thick (46 ± 4 km) crust that may be associated with such a root is only observed beneath the middle of the TAMNNET transect (Figure 6, Profile 1), and it does not continue to the south (Figure 6, Profile 2). This is inconsistent with plateau collapse and the associated uplift models put forth by *Studinger et al*. [2004] and *Bialas et al*. [2007]. The *Lawrence et al*. [2006a] model may be consistent with the current observations, where a small root could locally contribute to higher elevations, but this would not be an applicable model for the entire TAMs. Instead, small variations in crustal thickness, such as those observed between the TAMNNET and TAMSEIS transects, are more likely associated with local topographic variability.

Generally, both the current study and *Hansen et al.* [2009] indicate fairly uniform crustal thickness (~42–44 km) beneath the TAMs, suggesting that there is little along-strike variability in the crustal structure beneath the mountain range. *Stern and ten Brink* [1989] indicated that a uniform, ~45 km thick crust is consistent with a flexural uplift model for the TAMs. Additionally, this model indicates that the lithospheric thickness would be thinner near the coast, at the free edge of the East Antarctic plate [*Stern and ten Brink*, 1989; *ten Brink and Stern*, 1992; *ten Brink et al.*, 1997], and as is seen from the examined profiles (Figure 6, Profile 2), the current observations also agree well with this aspect of the flexure model. A flexural origin can also explain the structure of the WSB, where the basin is a down-warp caused by the uplift of the TAMs. The predicted crustal thickness beneath the WSB from the flexural model (~45 km) [*Stern and ten Brink*, 1989; *ten Brink and Stern*, 1992; *ten Brink et al.*, 1997; *van Wijk et al.*, 2008] agrees well with the average Moho depth beneath the basin found in our results (~41 km). Other formation mechanisms for the TAMs indicate thinner crust beneath the WSB (~31–35 km) [*Ferraccioli et al.*, 2001; *Studinger et al.*, 2004; *Lawrence et al.*, 2006a] and are less consistent with our findings.

The thermal load required by the flexural uplift model has also been supported by previous tomographic studies [*Bannister et al.*, 2000; *Morelli and Danesi*, 2004; *Watson et al.*, 2006; *Lawrence et al.*, 2006b], which show slow and presumably hot upper mantle beneath West Antarctica, adjacent to the TAMs near Ross Island and extending under the TAMs front. Recent results from *Hansen et al.* [2014] and *Graw et al.* [2014] based on the TAMNNET data suggest these slow, hot mantle perturbations continue beneath the northern TAMs as well. From the current study, noticeably slower crustal velocities are observed beneath the coastal KOPRI stations (Figure 7), which is noteworthy since this area coincides with the slow, warm upper mantle imaged in these previous studies. It is possible that the warm upper mantle temperatures may also affect crustal velocities. That is, the crust may be slowly heated and weakened by this upper mantle heat source, thus lowering the associated seismic velocity. Taking all of these observations into account, our crustal estimates best support a flexural model for the formation of the TAMs and the WSB.

6. Conclusions

Using data from the newly deployed TAMNNET array and stations operated by KOPRI, this study has estimated the crustal thickness and $\overline{V}_s$ beneath the northern TAMs and WSB with SRFs and Rayleigh wave phase velocities. Our findings provide new constraints on the crustal structure beneath a previously unexplored portion of the mountain range and the adjacent basin. Crust is thin (~20 km) near the Ross Sea coast but is consistently thicker (~41 km) inland beneath the WSB. A crustal thickness of ~46 km is observed beneath the highest elevations in the northern TAMs, but this increased thickness is not continuous along-strike of the mountain range. Average crustal shear velocities range from ~3.1 to 3.9 km/s, with slower velocities found near the Ross Sea coastline. Our results are most consistent with a flexural model for the TAMs and the WSB, associated with broad flexure of the East Antarctic lithosphere and uplift along its western, rifted edge due to lateral heat conduction from hotter mantle beneath West Antarctica [*Stern and ten Brink*, 1989; *ten Brink and Stern*, 1992; *ten Brink et al.*, 1997]. Locally, thicker crust beneath the TAMNNET transect may explain the additional topography in the northern TAMs compared to that seen in the central TAMs, near Ross Island.

References

Ammon, C. J. (1991), The isolation of receiver effects from teleseismic *P* waveforms, *Bull. Seismol. Soc. Am.*, *81*(6), 2504–2510.

Ammon, C. J., G. E. Randall, and G. Zandt (1990), On the nonuniqueness of receiver function inversions, *J. Geophys. Res.*, *95*(B10), 15,303–15,318, doi:10.1029/JB095iB10p15303.

Armienti, P., C. Ghezzo, F. Innocenti, P. Manetti, S. Rocchi, and S. Tonarini (1990), Isotope geochemistry and petrology of granitoid suites from Granite Harbour Intrusives of the Wilson Terrane, North Victoria Land, Antarctica, *Eur. J. Mineral.*, *2*, 103–123.

Bannister, S., R. K. Snieder, and M. L. Passier (2000), Shear-wave Velocities under the Transantarctic Mountains and Terror Rift from Surface Wave Inversion, *Geophys. Res. Lett.*, *27*(2), 281–284, doi:10.1029/1999GL010866.

Bannister, S., J. Yu, B. Leitner, and B. L. N. Kennett (2003), Variations in crustal structure across the transition from West to East Antarctica, Southern Victoria Land, *Geophys. J. Int.*, *155*(3), 870–884, doi:10.1111/j.1365-246X.2003.02094.x.

Bialas, R. W. (2009), Models of continental extension and exhumation: Influence of plateau collapse, sedimentation, dike injection, and slab rollback, *PhD Dissertation*, Columbia Univ., New York.

Bialas, R. W., W. R. Buck, M. Studinger, and P. G. Fitzgerald (2007), Plateau collapse model for the Transantarctic Mountains-west Antarctic Rift System: Insights from numerical experiments, *Geology*, *35*(8), 687–690, doi:10.1130/G23825A.1.

Blankenship, D. D., S. D. Kempf, and D. A. Young (2013), *IceBridge HiCARS 1L2 Geolocated Ice Thickness*, NASA National Snow and Ice Data Center, Boulder, Colo.

Burrett, C. F., and R. H. Findlay (1984), Cambrian and Ordovician conodonts from the Robertson Bay Group, Antarctica, and their tectonic significance, *Nature*, *307*, 723–725.

Drewry, D. J. (1976), Sedimentary basins of the East Antarctic craton from geophysical evidence, *Tectonophysics*, *36*(1–3), 301–314, doi:10.1016/0040-1951(76)90023-8.

Efron, B., and R. Tibshirani (1991), Statistical data analysis in the computer age, *Science*, *253*, 390–395.

Enright, K. (2010), *America's Natural Places: Rocky Mountains and the Great Plains*, Greenwood Publishing Group, Santa Barbra, Calif.

Farra, V., and L. Vinnik (2000), Upper mantle stratification by *P* and *S* receiver functions, *Geophys. J. Int.*, *141*(3), 699–712, doi:10.1046/j.1365-246x.2000.00118.x.

Federico, L., L. Crispini, G. Capponi, and J. D. Bradshaw (2009), The Cambrian Ross Orogeny in northern Victoria Land (Antarctica) and New Zealand: A synthesis, *Gondwana Res.*, *15*(2), 188–196, doi:10.1016/j.gr.2008.10.004.

Ferraccioli, F., F. Coren, E. Bozzo, C. Zanolla, S. Gandolfi, I. Tabacco, and M. Frezzotti (2001), Rifted(?) Crust at the East Antarctic Craton margin: Gravity and magnetic interpretation along a traverse across the Wilkes Subglacial Basin Region, *Earth Planet. Sci. Lett.*, *192*(3), 407–421, doi:10.1016/S0012-821X(01)00459-9.

Ferraccioli, F., E. Armadillo, T. Jordan, E. Bozzo, and H. Corr (2009), Aeromagnetic exploration over the East Antarctic Ice Sheet: A new view of the Wilkes Subglacial Basin, *Tectonophysics*, *478*(1–2), 62–77, doi:10.1016/j.tecto.2009.03.013.

Finotello, M., A. Nyblade, J. Julia, D. Wiens, and S. Anandakrishnan (2011), Crustal V_p-V_s ratios and thickness for Ross Island and the Transantarctic Mountain front, Antarctica, *Geophys. J. Int.*, *185*, 85–92, doi:10.1111/j.1365-246X.2011.04946.x.

Fitzgerald, P. G. (2002), Tectonics and landscape evolution of the Antarctic plate since the breakup of Gondwana, with an emphasis on the West Antarctic Rift System and the Transantarctic Mountains, *Roy. Soc. N.Z. Bull.*, *35*, 453–469.

Fitzgerald, P. G., M. Sandiford, P. J. Barrett, and A. J. W. Gleadow (1986), Asymmetric extension associated with uplift and subsidence in the Transantarctic Mountains and Ross Embayment, *Earth Planet. Sci. Lett.*, *81*, 67–78, doi:10.1016/0012-821X(86)90101-9.

Fitzgerald, P. G., R. Bialas, W. R. Buck, and M. Studinger (2007), A plateau collapse model for the formation of the West Antarctic Rift System/Transantarctic Mountains, *Int. Symp. Ant. Earth Sci.*, Abstract 4.A.B-5.

Forsyth, D. W., and A. Li (2005), Array analysis of two-dimensional variations in surface wave phase velocity and azimuthal anisotropy in the presence of multipathing interference, in *Seismic Earth: Array Analysis of Broadband Seismograms*, *Geophys. Monogr. Ser.*, vol. 157, pp. 81–97.

Fretwell, P., H. D. Pritchard, D. G. Vaughan, and B. Consortium (2013), Bedmap2: Improved ice bed, surface and thickness datasets for Antarctica, *Cryosphere*, *7*(1), 375–393, doi:10.5194/tc-7-375-2013.

Graw, J. H., S. E. Hansen, and A. Adams (2014), Upper mantle shear wave velocity structure beneath the Transantarctic Mountains and Eastern Wilkes Subglacial Basin, *Geol. Soc. Am. Conf.*, Abstract 246667.

Hansen, S. E., J. Julià, A. A. Nyblade, M. L. Pyle, D. A. Wiens, and S. Anandakrishnan (2009), Using *S* wave receiver functions to estimate crustal structure beneath ice sheets: An application to the Transantarctic Mountains and East Antarctic Craton, *Geochem. Geophys. Geosyst.*, *10*, Q08014, doi:10.1029/2009GC002576.

Hansen, S. E., A. A. Nyblade, D. S. Heeszel, D. A. Wiens, P. Shore, and M. Kanao (2010), Crustal structure of the Gamburtsev Mountains, East Antarctica, from *S*-wave receiver functions and Rayleigh wave phase velocities, *Earth Planet. Sci. Lett.*, *300*(3–4), 395–401, doi:10.1016/j.epsl.2010.10.022.

Hansen, S. E., J. H. Graw, L. M. Kenyon, A. A. Nyblade, D. A. Wiens, R. C. Aster, A. D. Huerta, S. Anandakrishnan, and T. Wilson (2014), Imaging the Antarctic mantle using adaptively parameterized *P*-wave tomography: Evidence for heterogeneous structure beneath West Antarctica, *Earth Planet. Sci. Lett.*, *408*, 66–78, doi:10.1016/j.epsl.2014.09.043.

Hansen, S. E., A. M. Reusch, T. Parker, D. K. Bloomquist, P. Carpenter, J. H. Graw, and G. R. Brenn (2015), The Transantarctic Mountains Northern Network (TAMNNET): Deployment and performance of a seismic array in Antarctica, *Seismol. Res. Lett.*, *86*, doi:10.1785/0220150117.

Huerta, A. D., and D. L. Harry (2007), The transition from diffuse to focused extension: Modeled evolution of the West Antarctic Rift system, *Earth Planet. Sci. Lett.*, *255*(1–2), 133–147, doi:10.1016/j.epsl.2006.12.011.

Julià, J., R. B. Herrmann, C. J. Ammon, and A. Akinci (2004), Evaluation of deep sediment velocity structure in the New Madrid Seismic Zone, *Bull. Seismol. Soc. Am.*, *94*(1), 334–340, doi:10.1785/0120030081.

Karner, G. D., M. Studinger, and R. E. Bell (2005), Gravity anomalies of sedimentary basins and their mechanical implications: Application to the Ross Sea basins, West Antarctica, *Earth Planet. Sci. Lett.*, *235*, 577–596.

Kim, K. Y., M. H. Hong, J. Lee, J. K. Hong, and Y. K. Jin (2007), Seismic experiments on the Fourcade Glacier in the King George Island, Antarctica, *Geophys. Res. Abs.*, 9, A-04755.

Kumar, P., et al. (2005), The lithosphere-asthenosphere boundary in the North-West Atlantic region, *Earth Planet. Sci. Lett.*, *236*(1–2), 249–257, doi:10.1016/j.epsl.2005.05.029.

Kyle, P. R., and J. W. Cole (1974), Structural controls of volcanism in the McMurdo volcanic Group, McMurdo Sound, Antarctica, *Bull. Volcanol.*, *38*, 16–35.

LaMasurier, W. E. (1990), Late Cenozoic volcanism on the Antarctic plate: An overview, in *Volcanoes of the Antarctic Plate and Southern Oceans*, *Antarct. Res. Ser.*, vol. 48, edited by W. E. LeMasurier and J. W. Thomson, pp. 1–17, AGU, Washington, D. C.

Langston, C. A. (1977), The effect of planar dipping structure on source and receiver responses for a constant ray parameter, *Bull. Seismol. Soc. Am.*, *67*(4), 1029–1050.

Langston, C. A. (1979), Structure under Mount Rainier, Washington, inferred from teleseismic body waves, *J. Geophys. Res.*, *84*(NB9), 4749–4762, doi:10.1029/JB084iB09p04749.

Last, R. J., A. A. Nyblade, C. A. Langston, and T. J. Owens (1997), Crustal structure of the East African Plateau from receiver functions and Rayleigh wave phase velocities, *J. Geophys. Res.*, *102*, 24,469–24,483, doi:10.1029/97JB02156.

Lawrence, J. F., D. A. Wiens, A. A. Nyblade, S. Anandakrishnan, P. J. Shore, and D. Voigt (2006a), Crust and upper mantle structure of the Transantarctic Mountains and surrounding regions from receiver functions, surface waves, and gravity: Implications for uplift models, *Geochem. Geophys. Geosyst.*, *7*, Q10011, doi:10.1029/2006GC001282.

Lawrence, J. F., D. A. Wiens, A. A. Nyblade S. Anandakrishnan, P. J. Shore, D. Voigt (2006b), Rayleigh wave phase velocity analysis of the Ross Sea, Transantarctic Mountains, and East Antarctica from a temporary seismograph array, *J. Geophys. Res.*, *111*, B06302, doi:10.1029/2005JB003812.

Li, X. Q., R. Kind, X. H. Yuan, I. Wolbern, and W. Hanka (2004), Rejuvenation of the lithosphere by the Hawaiian plume, *Nature*, *427*(6977), 827–829, doi:10.1038/nature02349.

Ligorria, J. P., and C. J. Ammon (1999), Iterative deconvolution and receiver-function estimation, *Bull. Seismol. Soc. Am.*, *89*(5), 1395–1400.

Lisker, F., and A. L. Laufer (2013), The Mesozoic Victoria Basin: Vanished link between Antarctica and Australia, *Geology*, *41*(10), 1043–1046, doi:10.1130/G33409.1.

Morelli, A., and S. Danesi (2004), Seismological imaging of the Antarctic continental lithosphere: A review, *Global Planet. Change*, *42*(1–4), 155–165, doi:10.1016/j.gloplacha.2003.12.005.

Park, Y., H. J. Yoo, W. S. Lee, J. Lee, Y. Kim, S. H. Lee, D. Shin, and H. Park (2014), Deployment and performance of a broadband seismic network near the New Korean Jang Bogo research station, Terra Nova Bay, East Antarctica, *Seismol. Res. Lett.*, *85*, 1341–1347.

Pyle, M. L., D. A. Wiens, A. A. Nyblade, and S. Anandakrishnan (2010), Crustal structure of the Transantarctic Mountains near the Ross Sea from ambient seismic noise tomography, *J. Geophys. Res.*, *115*, B11310, doi:10.1029/2009JB007081.

Robinson, E. S., and J. F. Splettstoesser (1984), Structure of the Transantarctic Mountains determined from geophysical surveys, in *Geology of the Central Transantarctic Mountains*, *Ant. Res. Ser.*, vol. 36, pp. 119–162.

Rossetti, F., F. Tecce, L. Aldega, M. Brilli, and C. Faccenna (2006), Deformation and fluid flow during orogeny at the palaeo-Pacific active margin of Gondwana: The Early Paleozoic Robertson Bay accretionary complex (north Victoria Land, Antarctica), *J. Metamorph. Geol.*, *24*, 33–53.

Stern, T. A., and U. S. ten Brink (1989), Flexural uplift of the Transantarctic Mountains, *J. Geophys. Res.*, *94*(B8), 10,315–10,330, doi:10.1029/JB094iB08p10315.

Storti, F., M. L. Balestrieri, F. Balsamo, and F. Rossetti (2008), Structural and thermochronological constraints to the evolution of the West Antarctic Rift System in central Victoria Land, *Tectonics*, *27*, TC4012, doi:10.1029/2006TC002066.

Studinger, M., R. E. Bell, W. R. Buck, G. D. Karner, and D. D. Blankenship (2004), Sub-ice geology inland of the Transantarctic Mountains in light of New aerogeophysical data, *Earth Planet. Sci. Lett.*, *220*(3–4), 391–408, doi:10.1016/s0012-821x(04)00066-4.

Stump, E. (1992), The Ross Orogen of the Transantarctic Mountains in the light of the Laurentia-Gondwana split, *GSA Today*, *2*, 25–28.

Stump, E., M. G. Laird, J. D. Bradshaw, J. R. Holloway, S. G. Borg, and K. E. Lapham (1983), Bowers graben and associated tectonic features cross northern Victoria Land, Antarctica, *Nature*, *304*, 334–336.

ten Brink, U. S., and T. Stern (1992), Rift flank uplifts and Hinterland Basins: Comparison of the Transantarctic Mountains with the Great Escarpment of South Africa, *J. Geophys. Res.*, *97*(B1), 569–585, doi:10.1029/91JB02231.

ten Brink, U. S., S. Bannister, B. C. Beaudoin, and T. A. Stern (1993), Geophysical investigations of the tectonic boundary between East and West Antarctica, *Science*, *261*(5117), 45–50.

ten Brink, U. S., R. I. Hackney, S. Bannister, T. A. Stern, and Y. Makovsky (1997), Uplift of the Transantarctic Mountains and the bedrock beneath the East Antarctic ice sheet, *J. Geophys. Res.*, *102*(B12), 27,603–27,621, doi:10.1029/97JB02483.

Turcotte, D. L., and G. Schubert (2002), *Geodynamics*, 2nd ed., Cambridge Univ. Press, New York.

van Wijk, J. W., J. F. Lawrence, and N. W. Driscoll (2008), Formation of the Transantarctic Mountains related to extension of the West Antarctic Rift system, *Tectonophysics*, *458*, 117–126.

Watson, T., A. Nyblade, D. A. Wiens, S. Anandakrishnan, M. Benoit, P. J. Shore, D. Voight, and J. VanDecar (2006), *P* and *S* velocity structure of the upper mantle beneath the Transantarctic Mountains, East Antarctic Craton, and Ross Sea from travel time tomography, *Geochem. Geophys. Geosyst.*, *7*, Q07005, doi:10.1029/2005GC001238.

Weaver, S. D., J. D. Bradshaw, and M. G. Laird (1984), Geochemistry of Cambrian volcanics in northern Victoria Land, Antarctica, *Earth Planet. Sci. Lett.*, *68*, 128–140.

Wilson, D. C., D. A. Angus, J. F. Ni, and S. P. Grand (2006), Constraints on the interpretation of *S*-to-*P* receiver functions, *Geophys. J. Int.*, *165*(3), 969–980, doi:10.111/j.1365-246X.2006.02981.x.

Zelt, B. C., and R. M. Ellis (1999), Receiver-function studies in the Trans-Hudson Orogen, Saskatchewan, *Can. J. Earth Sci.*, *36*(4), 585–603, doi:10.1139/e98-109.

Zhu, L. P., and H. Kanamori (2000), Moho depth variation in southern California form teleseismic receiver functions, *J. Geophys. Res.*, *105*(B2), 2969–2980, doi:10.1029/1999JB00322.